Analysis of Local Fracture Strain and Damage Limit of Advanced High Strength Steels using Measured Displacement Fields and FEM

N. Ma[1,2], K. Sato[3] and K. Takada[4]

Abstract: The local mechanical behaviors of advanced high strength steels undergoing a very large strain from uniform plastic deformation to fracture were investigated with the aid of a measured displacement field and a measurement based FEM. As a measurement method, a digital image grid method (DIGM) was developed and the three-direction transient displacement field on uniaxial tensile test pieces was measured. Combining the measured transient displacement field with the finite element method, a measurement based FEM (M-FEM) was developed for the computation of distribution of the local strains, local stresses and ductile damage accumulation in a tensile test piece. Furthermore, the local fracture strain and damage limit of several advanced high strength steel sheets (980MPa/t1.2mm, 980MPa/t1.6mm, 1180MPa/t1.6mm) were identified by uniaxial tensile tests and the measurement based FEM. The identified damage limit of materials agreed very well compared with that measured by a conventional press test, and the validity of the measuring method and measurement based FEM was verified.

Keywords: Digital image grid method, Measured displacement field, Measurement based FEM, Local fracture strain, Damage limit, Advanced high strength steels.

1   Introduction

The finite element method (FEM) has been widely used in the analysis of mechanical behaviors of various materials and structures. To know the detail distribution of the local strains and stresses by FEM, the analyzing object is generally divided into very small elements. However, the local strains and stresses in a small element were difficult to be measured by conventional experiments.

---

[1] Osaka University, Osaka, Japan.
[2] JSOL Corporation, Osaka, Japan.
[3] JFE Steel Corporation, Hiroshima, Japan.
[4] Honda R&D Co. Ltd, Tochigi, Japan.

Recently, with the aid of advanced measurement methods such as a digital image correlation method, the local mechanical deformation behaviors in materials can be directly observed by experiments. These directly measuring technologies are very helpful in developing some new computational methods and also in verifying the numerical simulation models.

A digital image correlation method (DIC) was early developed by Peters et al. (1981), Chu et al. (1985), and Sutton et al. (1986). Pan et al. (2009) reviewed the measuring technology of DIC for strain field in details. Huang et al. (2011) evaluated the anisotropic parameter R-value; Zeng and Xia (2010) determined stress-strain curve beyond uniform elongation. Based on DIC based measuring methods, Ramazani et al. (2013) investigated deformation characterization of failure initiation in a dual phase steel; Paul (2012) predicted failure modes of dual phase steels. Coppieters et al. (2014) measured the large strains using the digital image correlation method and identified post-necking strain hardening phenomena. In this year, Hopmann et al. (2015) measured the strain rate dependent material properties of polymers and Sato et al. (2015) measured the strain rate dependent fracture behaviors of advanced high strength steels, Jian et al. (2015) investigated the damage initiation of dual phase steels under different stress triaxiality.

Up to now, experimental measurements and numerical simulations using FEM were performed independently. Their seamless combination was not deeply discussed. An early application of their combination was tried by Ueda et al. (1989) who computed the distributions of three dimensional internal welding residual stresses by elastic FEM using measured released strains. Recently, great attentions are being paid to the applications of the displacement field measured by digital image correlation method. Besnard et al. (2006) developed a method to estimate the displacement from a pair of images and evaluated the displacement field for finite-element analysis. Dupuy et al. (2010) mapped the measured displacement field to finite element model and analyzed elastic bending behaviors on single shear lap joint. Tarigopula et al. (2008) extended DIC to the study of large plastic deformation problem. Furthermore, Roux and Hild (2008) estimated the damage using measured results by DIC. Yoneyama (2011) developed a smoothing scheme for measured displacements and then calculated the strain concentration around a hole in a plate specimen.

Generally, the digital image correlation method is based on a random pattern painted on the surface of structure samples. The painted random pattern is easy to be broken and accompanied measuring errors may increase when the deformation becomes large. Ma et al. (2014) developed a digital image grid method (DIGM) using a regular pattern with grids etched electrochemically on the surface of a test piece. The grids etched electrochemically on the surface of test pieces can suffer a very large

deformation until fracture. The regular patterns used in DIGM can be arranged as a rectangle shape or a triangle shape which is similar to the element shape of FEM. The grids of regular patterns can be used as the nodes of FEM. These grids can also be modelled by particles if the meshless local petrov-galerkin method (MLPG) [Liu et al. (2006), Sladeki et al. (2013)] is employed. Recently, an advanced MLPG-Eshelby Method was proposed by Han and Atluri (2014) which has advantages to deal with material separation. If the measured displacement fields are combined with MLPG-Eshelby Method in the future work, the detailed fracture behaviors such as crack initiation and propagation will be investigated.

In the present article, the digital image grid method (DIGM) with regular patterns was used to measure the transient displacement field of tensile test pieces during loading process. Then, the measured grid displacements are considered as the nodal displacements in widely employed FEM, and the strains and stresses can be directly estimated. This combination is here named as a measurement based finite element method (M-FEM). Then applications of M-FEM to the computation of distribution of the local strains, the local stresses and the local ductile damage accumulation in steel materials during tensile tests are represented. Furthermore, the ductile damage limit of several advanced high strength steels was identified by the proposed M-FEM. The identified damage limit agreed well with the value measured by a conventional method and the validity of M-FEM was verified.

2 Displacement field measurement by digital image grid method

2.1 Digital image grid method (DIGM)

The digital image grid method used in the uniaxial tensile test is schematically shown in Fig. 1(a). It consists of a two-camera system for static tensile testing which is controlled by a computer. The specifications of the digital cameras used in the experiments are shown in Fig. 1(b). The digital images were taken every 2.0 sec in the tensile test. The grids with a diameter of 0.25 mm or 0.5 mm are electrically etched with a certain pitch length named as grid pitch length. The grid pitch length can be 0.5mm or 1.0mm or 2.0mm as shown in Fig. 1(c) depending on the measuring requests. The size of grids and grid pitch length are designed by considering the limitation of the degree of etching precision and accuracy for the local strain measurement. The center of the grid was determined by the fitting of elliptic curves from each image. Using the digital image correlation method, the center of the distorted grids was determined accurately even a large distortion occurs after the strain localization. The 3D coordinates of the grids on the specimen were calculated using the center of the fitted ellipses. The three displacement components u_x, u_y, u_z at the grids were calculated from the coordinate changes in

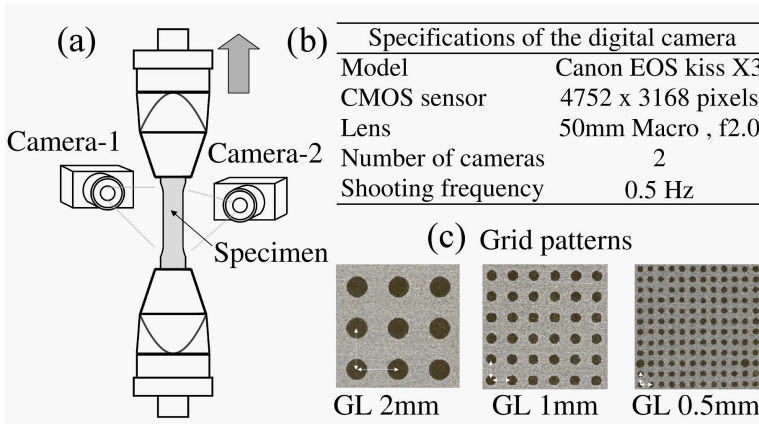the x, y and z directions, which were continuously measured within a certain time interval.

Figure 1: Measuring system of digital image grid method: (a) Static tensile test machine with two digital cameras, (b) Specifications of the digital camera, (c) conditions of the grid pitch length and grid size.

In the digital image grid method, the deformation of the etched grids on the specimen is analyzed using a computer vision algorithm (2006). The computer vision algorithm is able to reconstruct a three-dimensional (3D) shape from multiple two-dimensional (2D) images. The relationship between a 3D-coordinate point, $M(x, y, z)$ in the three dimensional global coordinate system and a point $m(u, v)$ in the two dimensional camera coordinate system is represented by Eq. (1).

$$\lambda \cdot m = A[R|T]M \tag{1}$$

where λ is a scale parameter, **A** is a camera matrix including the focal length (a_u, a_v), the center of the image (u_0, v_0), and a share factor scale, s. The **R** and **T** matrixes are the transformation and rotation matrixes defined by Eq. (2) and shown in Figure 2 respectively

$$A = \begin{bmatrix} a_u & s & u_0 \\ 0 & a_v & v_0 \\ 0 & 0 & 1 \end{bmatrix}, \quad R = \begin{bmatrix} r_{11} & r_{12} & r_{13} \\ r_{21} & r_{22} & r_{23} \\ r_{31} & r_{32} & r_{33} \end{bmatrix}, \quad A = \begin{Bmatrix} T_x \\ T_y \\ T_z \end{Bmatrix} \tag{2}$$
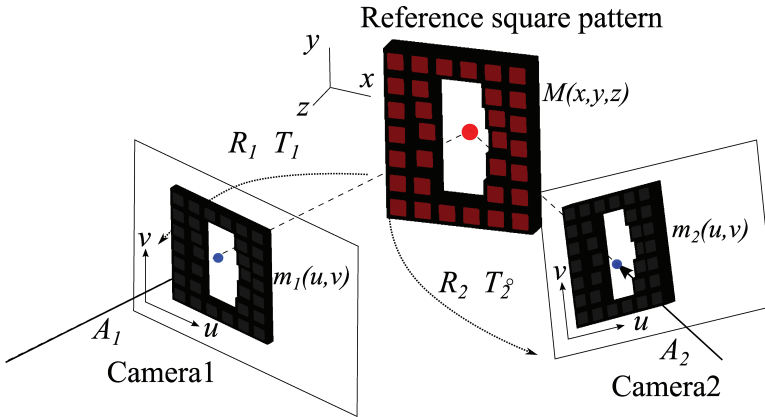
Figure 2: Rotation and translation of the stereo camera model.

In the Eq. (1), the part of $A\,[R|T]$ is condensed into a 3×4 matrix, P, as follows

$$\lambda \left\{ \begin{array}{c} u \\ v \\ 1 \end{array} \right\} = \left[\begin{array}{cccc} P_{11} & P_{12} & P_{13} & P_{14} \\ P_{21} & P_{22} & P_{23} & P_{24} \\ P_{31} & P_{32} & P_{33} & P_{34} \end{array} \right] \left\{ \begin{array}{c} x \\ y \\ z \\ 1 \end{array} \right\} \tag{3}$$

The parameters of the camera matrix P can be estimated using a pattern with known 3D coordinate points and the projected points in the camera coordinate system shown in Fig. 2. Once P is determined, the transformation and rotation of the camera are calculated by the decomposition of matrix P. When the positions and rotations of all cameras are calculated, the 3D position of the object can be calculated from multiple images captured by the cameras. The calculation problem is a linear simultaneous equation with 3D-coordinate parameters x, y and z. The equation could be solved using the inverse matrix of P.

2.2 Measuring object

Figure 3 shows a uniaxial tensile test piece of a high strength steel sheet 980MPa with 1.6mm in thickness and the displacement field on the highlight area was measured by the digital image grid method. The marks ● are the grids used in DIGM where the displacements are to be continuously measured.

2.3 Displacement field measured by DIGM

When the length of the measuring area of a tensile test piece of a steel sheet 980MPa/t1.6mm is pulled from the original 52.7711mm to 61.289mm with a con-
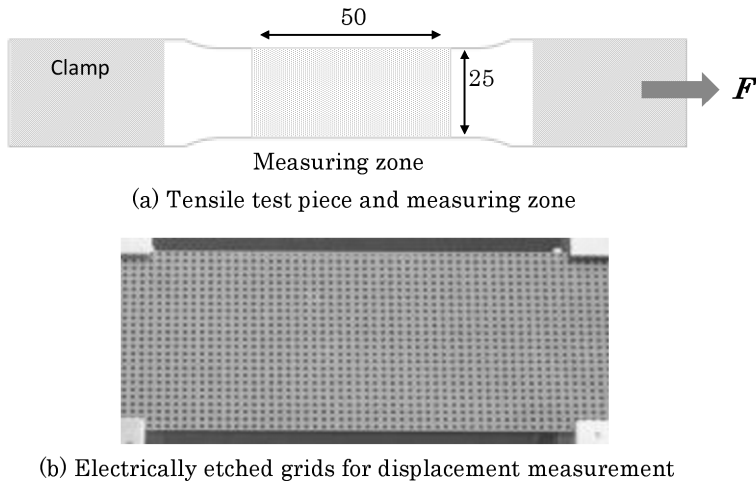
(a) Tensile test piece and measuring zone

(b) Electrically etched grids for displacement measurement

Figure 3: A tensile test piece and the grids for displacement measurement by DIGM.

trolled velocity 2.5mm/min, the displacement field of component Ux in the tensile direction (x) directly measured by DIGM with grid pitch length 1.0mm is shown in Figure 4. The points marked by ◯, ◇ and □ are the focused points located at edges and center of the tensile test piece. The distribution of the measured displacement component Uy in the transverse direction (y) is shown in Figure 5. The obvious necking in the width direction of a tensile test piece can be observed. The measured necking displacement Uy at the two edges of the width direction (y) has a little difference. The distribution of displacement component Uz in the thickness direction (z) is shown in Figure 6. The through thickness necking can be obviously observed at the center of a test piece in the width direction.

Figure 7 shows the history of measured displacements Ux, Uy and Uz at the three points marked by ◯(upEdge), ◇(lowEdge) and □(Center), respectively. Among the three displacement components, the tensile directional displacement component Ux is largest. The value of the measured displacement Ux at three points has a little difference. The deformation directions of the displacement Uy between the two points located at the up edge and low edge, respectively, are opposite, and the value at the up edge point is larger than that at the low edge point. The displacement Uz at the two edge points is almost the same and that at the center point is quite different.

From the directly measured displacement fields of components Ux, Uy and Uz shown in Figures 4-7, it can be seen that the distribution of displacements along the

width direction of the tensile test piece is not symmetric because the experimental conditions are not as simple as the conditions used in the standard FEM. Therefore, the combination of the directly measured displacement fields with FEM should play a very important role in investigating the practical deformation behaviors occurred in experiments.
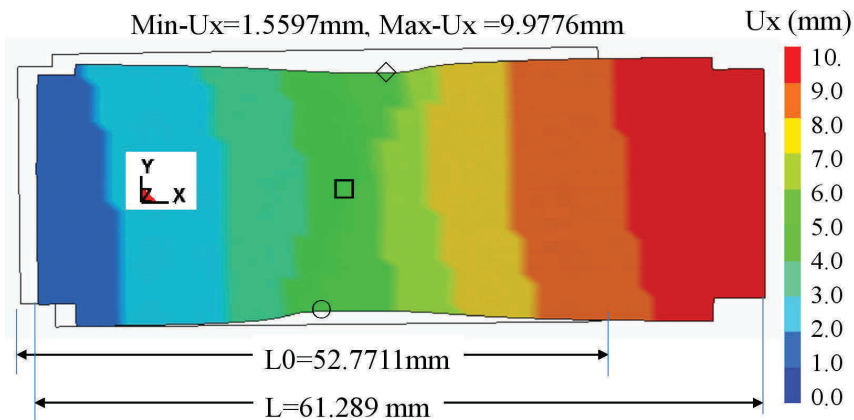
Min-Ux=1.5597mm, Max-Ux =9.9776mm   Ux (mm)

L0=52.7711mm

L=61.289 mm

Figure 4: Distribution of measured displacement component Ux(mm)

Min-Uy=-1.9245mm, Max-Uy =1.1853mm   Uy (mm)
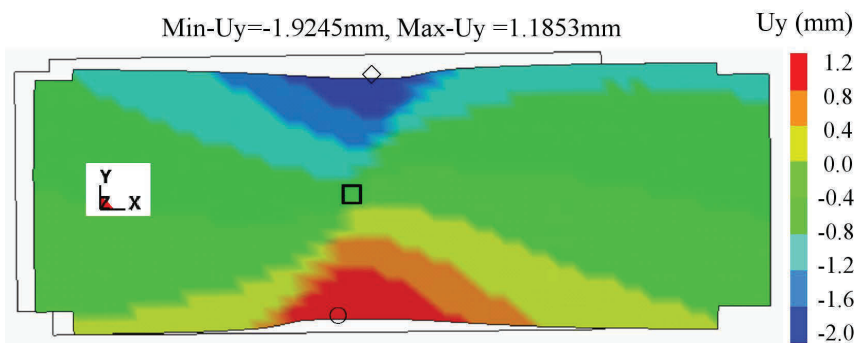
Figure 5: Distribution of measured displacement component Uy(mm)

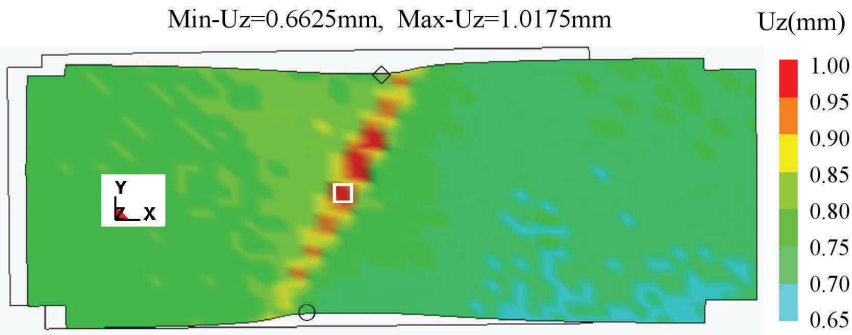Min-Uz=0.6625mm, Max-Uz=1.0175mm   Uz(mm)

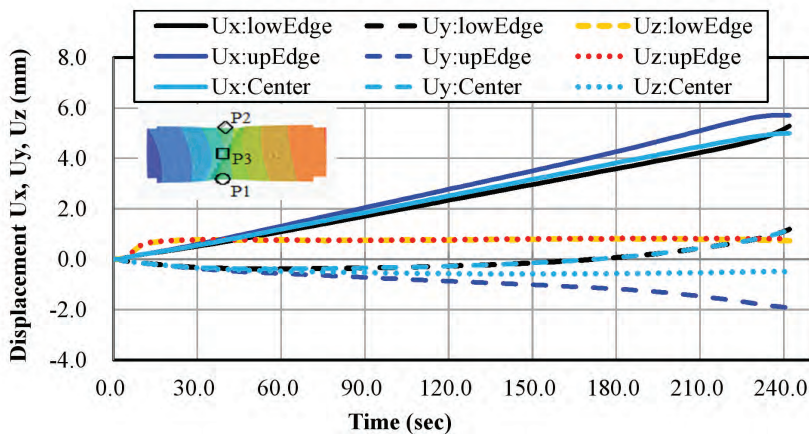Figure 6: Distribution of measured displacement component Uz(mm)

Figure 7: History of measured displacements Ux, Uy and Uz at two edges and center

3   Measurement based FEM for local strains, stresses and damage computation

The standard FEM for nonlinear problems is based on Eq. (4) using the stiffness matrix [K] and nodal displacement increment $\{\Delta u(t)\}$ at time t if external nodal force increment $\{\Delta F(t)\}$ is applied to an analyzed model.

$$[K]\{\Delta u(t)\} = \{\Delta F(t)\} \tag{4}$$

If the nodal displacement increment $\{\Delta u(t)\}$ is obtained by solving Eq.(4), the total displacement $\{u(t)\}$ at nodes, the strain increment $\{\Delta \varepsilon(t)\}$, the total strain

$\{\varepsilon(t)\}$, the stress increment $\{\Delta\sigma(t)\}$ and the total stress $\{\sigma(t)\}$ in elements can be computed in sequence by Eqs.(5-9). Furthermore, the strength and damage accumulation of materials can be predicted.

$$\{u(t)\} = \{\Delta u(t - dt)\} + \{\Delta u(t)\} \tag{5}$$

$$\{\Delta\varepsilon(t)\} = [B]\{\Delta u\} \tag{6}$$

$$\{\varepsilon(t)\} = \{\varepsilon(t - dt)\} + \{\Delta\varepsilon(t)\} \tag{7}$$

$$\{\Delta\sigma(t)\} = [D^e](\{\Delta\varepsilon\} - \{\Delta\varepsilon^p\}) \tag{8}$$

$$\{\sigma(t)\} = \{\sigma(t - dt)\} + \{\Delta\sigma(t)\} \tag{9}$$

Where, [B] is the strain-displacement matrix depending on the element types used in FEM and $[D^e]$ is the elastic matrix of material defined by Young's modules and Poisson's ratio.

With the progress of measurement technologies, the nodal displacement increment $\{\Delta u(t)\}$ in Eq. (4) can be partially or fully measured. If the nodal displacement at partial nodes is measured and expressed by $\{\Delta\bar{u}\}$, the nodal displacement vector $\{\Delta u(t)\}$ of all nodes used in FEM can be classified into the unknown nodal displacement increment $\{\Delta u\}$ and known nodal displacement $\{\Delta\bar{u}\}$. Therefore, the basic Eq. (4) of the standard FEM can be transferred into Eq.(10) which can be called as a partial measurement based FEM.

$$\begin{bmatrix} K_{uu} & K_{u\bar{u}} \\ K_{\bar{u}u} & K_{\bar{u}\bar{u}} \end{bmatrix} \begin{Bmatrix} \Delta u \\ \Delta\bar{u} \end{Bmatrix} = \begin{Bmatrix} \Delta\bar{F} \\ \Delta F \end{Bmatrix} \tag{10}$$

Where, $\{\Delta\bar{F}\}$ is the applied external nodal force and $\{\Delta F\}$ is the reaction nodal force at the nodes where the nodal displacement is known by measurement. K_{uu}, $K_{u\bar{u}}$, $K_{\bar{u}u}$, $K_{\bar{u}\bar{u}}$ are the components of stiffness matrix corresponding to the unknown displacement $\{\Delta\bar{u}\}$ and the known displacement $\{\Delta\bar{u}\}$.

If the displacements $\{\Delta u\}$ at all the nodes of a FE model are measured, it is unnecessary to solve Eq. (10). The total displacement at nodes, strains and stresses in elements of FE models can be computed by Eqs. (5)-(9) using measured results. This method is here named as a measurement based FEM which can be used for detail evaluation of the local strains and stresses existing in materials.

Generally, the computation for strains and stresses by standard FEM is performed following the flow shown in Figure 8. If the displacement field at the interesting zones was measured, the computational flow based on the measurement based FEM for local strains and stresses in materials can be simply summarized by Figure 9. The main differences of the measurement based FEM from the standard FEM are

highlighted in Fig.9. One is that the mesh used in M-FEM must be correspond-
ing to the measuring points and another is that the nodal displacement increment
$\{\Delta u\}$ used in M-FEM is just the measured value. In the measurement based FEM,
the isotropic Mises yield function or the anisotropic Hill yield function can be em-
ployed. After the strains and stresses are computed, their damage variables in ele-
ments for strength evaluation can be also computed. In this study, a ductile damage
originally proposed by Cockcroft-Latham (1968) was mainly discussed, because it
has been successfully applied to prediction of the crack occurrence during metal
forming by Takuda et al. (2009) and to the impact strength evaluation by Takada et
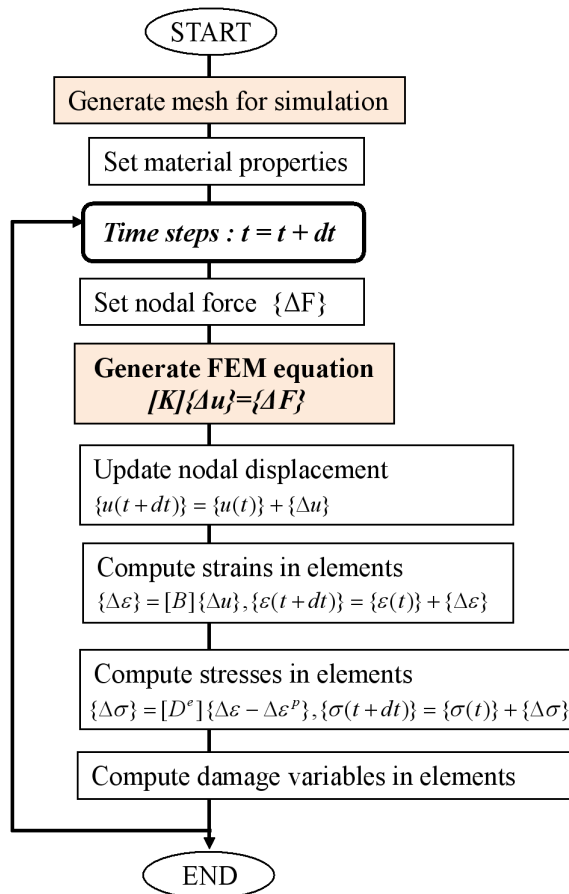al. (2015) after implemented into commercial software LS-DYNA by Ma (2013).
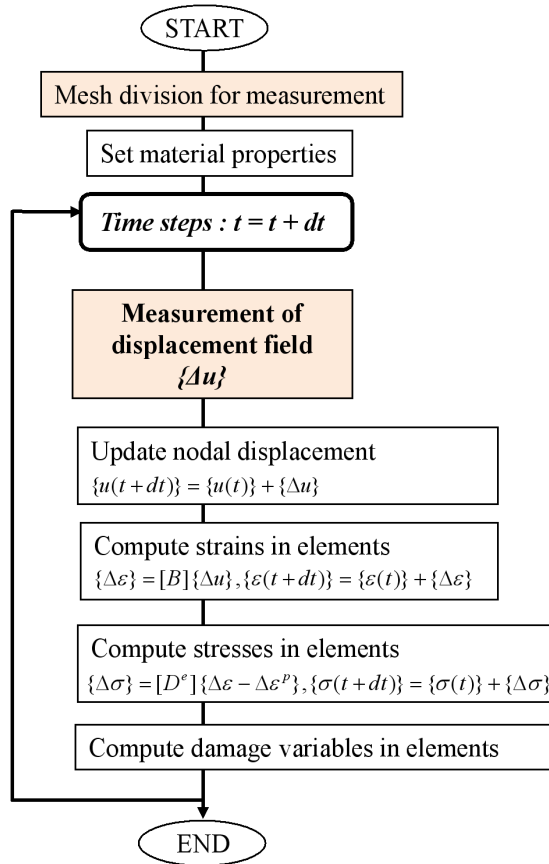

Figure 8: Flow of standard FEM.

START

Mesh division for measurement

Set material properties

Time steps : t = t + dt

Measurement of displacement field {Δu}

Update nodal displacement
$\{u(t+dt)\} = \{u(t)\} + \{\Delta u\}$

Compute strains in elements
$\{\Delta\varepsilon\} = [B]\{\Delta u\}, \{\varepsilon(t+dt)\} = \{\varepsilon(t)\} + \{\Delta\varepsilon\}$

Compute stresses in elements
$\{\Delta\sigma\} = [D^e]\{\Delta\varepsilon - \Delta\varepsilon^p\}, \{\sigma(t+dt)\} = \{\sigma(t)\} + \{\Delta\sigma\}$

Compute damage variables in elements

END

Figure 9: Flow of measurement based FEM.

4 Strain distributions and local fracture strain computed by M-FEM

4.1 Mesh division

To use the measurement based FEM, the measuring grids shown in Fig. 3 are defined as nodes and rectangle shell elements corresponding the measuring zone are generated as shown in Figure 10. The mesh size is equal to the grid pitch length 1.0mm used in the measurement. A plane stress state in the uniaxial tensile test piece is assumed and a membrane shell element with one integration point through the thickness direction was employed. Therefore, the measured in-plane components Ux and Uy were only applied to nodes of the analyzing model. The strain component ε_z in the thickness direction of shell elements is computed from in-plane strain components ε_x and ε_y.
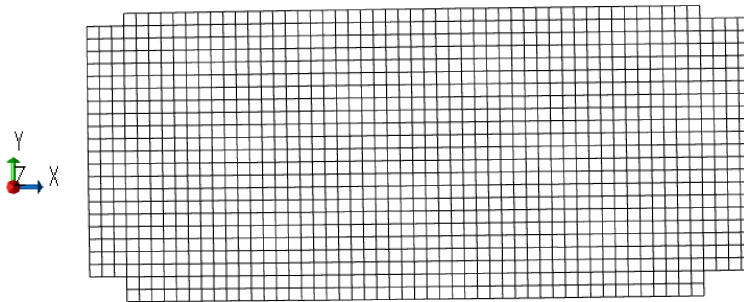
Figure 10: Shell elements corresponding to the measuring grids in DIGM.

4.2 *Local strain distributions*

Figure 11 and Figure 12 represent the distribution of the maximum in-plane principal strain (Major strain) and its deformation direction just before crack occurrence. A large tensile deformation band can be obviously observed. The vector direction of the major strain is approximately parallel to the tensile direction. The element located at the center of the large deformation band has a largest principal strain. The maximum local strain is about 0.62 just before cracking. In the other word, the local fracture strain 0.62 measured with 1.0mm gauge length is much larger than the elongation of 980MPa/t1.6mm steel sheet which is evaluated using 50mm gauge length.

Figure 13 and Figure 14 show the distribution of the minimum in-plane principal strain (Minor strain) and its deformation direction, respectively. A compressive deformation direction of the minor strain is approximately parallel to the width direction of the tensile test piece.

Figure 15 shows the thickness distribution just before crack occurrence. The center in the width direction of the tensile test piece has a thinnest thickness 1.14mm and the local thickness strain is about -33.4%.
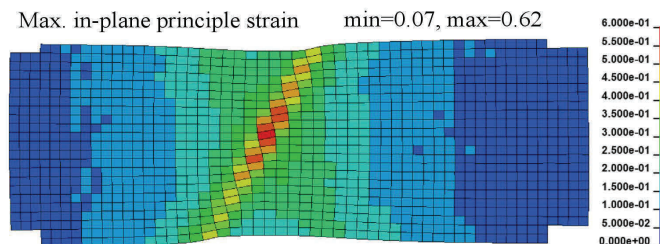

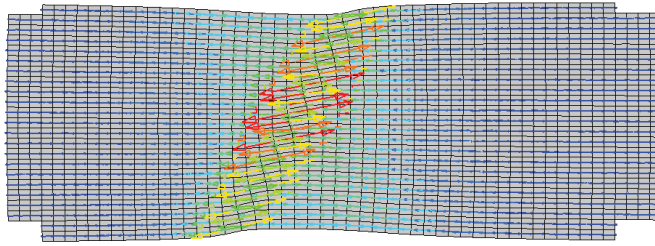Figure 11: Major strain distribution.
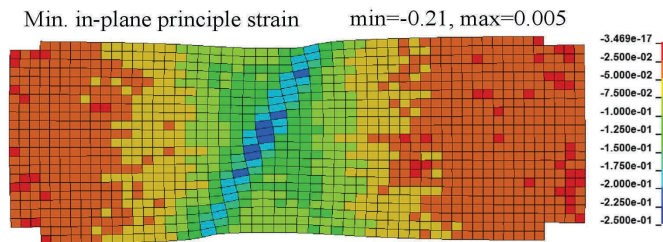
Figure 12: Major strain direction.

Figure 13: Minor strain distribution.

4.3 Local fracture strain

From the local strain distributions shown in Fig.11 and Fig.15, it has been known that the crack initiated at the center of the uniaxial tensile test piece. Referring to the FLD expression for crack estimation in sheet metal forming, the local in-plane principal strains (ε_1, ε_2) at the crack initiation element and their historical path up to fracture are shown in Figure 16. When the in-plane principal strains ε_1 and ε_2 are small, their relation i.e. the strain path is linear and its ratio β is about 0.5 representing the uniaxial stress state. When the strains become larger, the strain path curve changes its direction parallel to the vertical axis and the ratio β of the major strain increment $d\varepsilon_1$ and minor strain increment $d\varepsilon_2$ changes to near zero, which represents the plane strain state. The local fracture strain marked by $\times$ measured with the 1.0mm grid pitch length for steel 980MPa/t1.6mm is 0.62.

4.4 Local necking deformation characteristics

To investigate the local deformation characteristics, the local strains (ε_x, ε_y, ε_z) at the center of the transverse section where crack initiated in the uniaxial tensile tests and their change with strain-x over 50mm in gauge length which is equal to the tensile stroke if multiplied by 50mm, are shown in Figure 17. The broken red line in
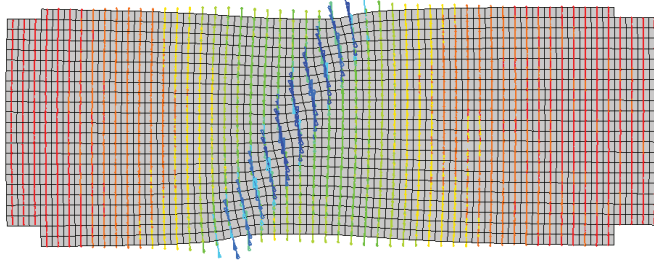
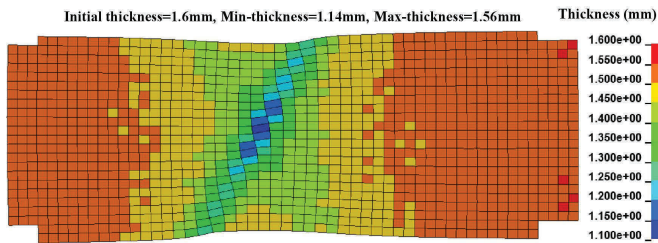Figure 14: Minor strain direction.

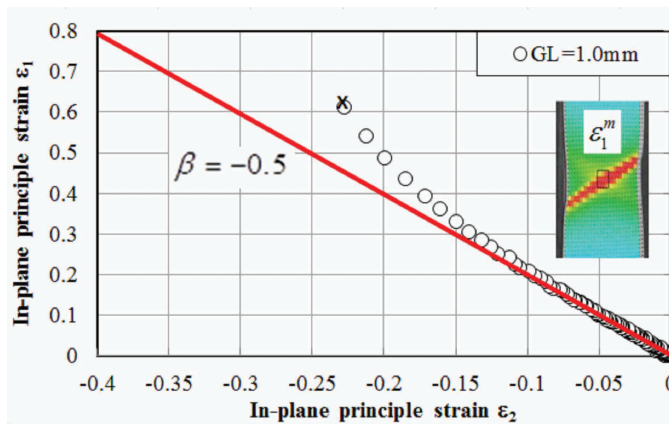Figure 15: Thickness distribution before crack occurrence.

Figure 16: Local strain path and local fracture strain of 980MPa/t1.6mm.

Fig.17 represents an assumed relation if the local strain ε_x was always equal to the average strain-x. When the average strain-x is less than about 0.08, the local strain ε_x is approximately equal to the average strain-x and it can be understood that the uniform deformation occurred. Below this value, the three local strain components ε_x, ε_y and ε_z have a linear relation with the average strain-x, and the difference between ε_y and ε_z is small. If a local strain ratio $d\varepsilon_y/d\varepsilon_z$ is given by Eq.(11) and named as a local anisotropic parameter R_{local} to evaluate the deformation characteristics, its value is close to 1.0 and the material has an isotropic deformation feature when the strain is small.

$$R_{local} = d\varepsilon_y/d\varepsilon_z = -d\varepsilon_y/(d\varepsilon_z + d\varepsilon_y) \tag{11}$$

When the average strain-x is larger than 0.08, the changes of the local strains ε_x, ε_y and ε_z with the average strain-x become nonlinear. If looking at the changes of the local strains in details, the changing tendency of the local strains ε_x, ε_y and ε_z is different when the average strain-x is between 0.08~0.13 and larger than 0.13. When the average strain-x is between 0.08 and 0.13, the local thickness strain ε_z changes a little bit larger than the local strain ε_y. From another view, the local strain ratio $d\varepsilon_y/d\varepsilon_z$ i.e. the local anisotropic parameter R_{local} becomes less than 1.0 and an anisotropic deformation occurred. When the average strain-x is larger than 0.13, the local thickness strain ε_z changes much faster than the local strain ε_y. This is because the through thickness necking occurred. This phenomenon can also be described by the decreasing change of the local anisotropic value R_{local} with local strain as shown in Figure 18. The R_{av} in Fig.18 which was measured from 50mm gauge length, is the conventional average anisotropic R-value for description of material anisotropic deformation, and is generally considered as a constant.

To clearly distinguish diffusion necking in the width direction and local necking in the thickness direction, Figure 19 shows the changes of local thinning strain ε_z at three locations (Center, upEdge, lowEdge) and average shrinkage strain ε_y in the width direction of the tensile test piece as drawn by purple broken line (ey : average of GL25mm). The red dotted line (ey : assumed uniform) in this figure was drawn to express the assumed isotropic uniform shrinkage. When the average strain-x with the gauge length GL50mm is less than 0.08, the thinning strain ε_z at all three locations and average shrinkage strain ε_y in the transverse direction (GL25mm) overlapped with the assumed isotropic uniform strain ε_y. When the average strain-x is between 0.8-0.13, the thinning strain ε_z at the three locations have a little difference. When the average strain-x is larger than 0.13, the thinning strain ε_z at the center increased much faster than that at the up edge and low edge. This means that the local necking and crack occurred at the center of the tensile test piece.
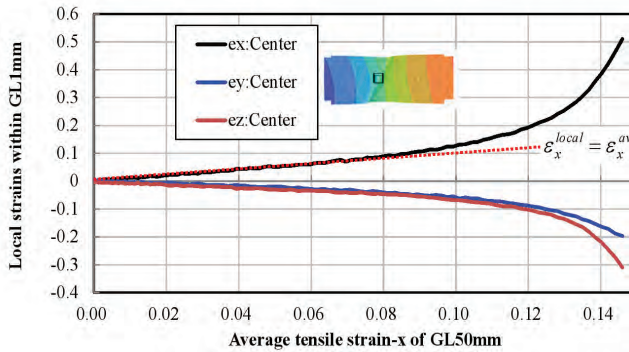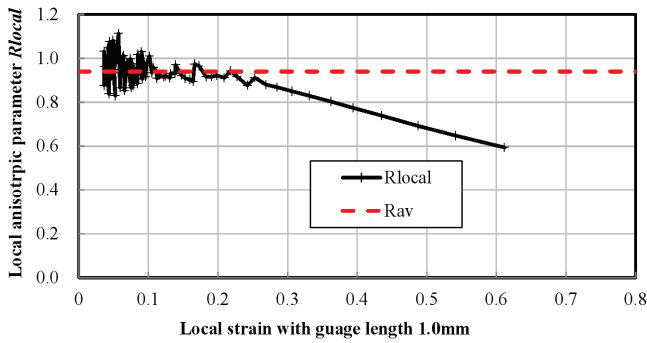
Figure 17: Changes of local strains.

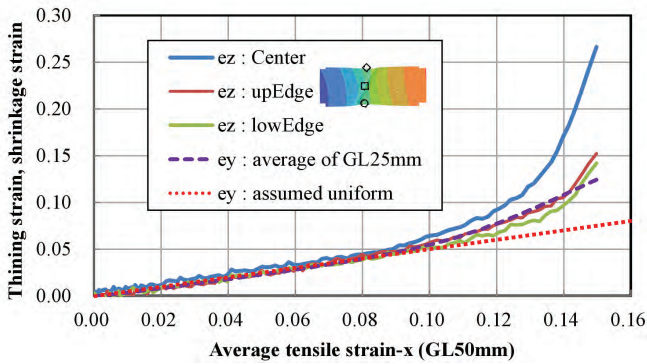Figure 18: Changes of local anisotropic value.

Figure 19: Historical change of thinning strain ez and shrinkage strain ey.

5 Stress distribution computed by M-FEM

To compute the stresses in the tensile test piece by M-FEM, the nonlinear stress and strain relation under plastic deformation state must be given or identified. Generally, the strain hardening phenomena are coupled with yield function and stress cycles. In this uniaxial tensile test, kinematic hardening is not considered because there is no unloading process. For steel materials, the Hill yield function is often selected for the description of stresses and strains under the plasticity state. Therefore, the Hill yield function with averaged anisotropic value r=0.94 for a 980MPa/t1.6mm steel sheet is here employed. Furthermore, a uniaxial tensile test piece as shown in Figure 20(a) was modeled by finite element with 1.0mm in mesh size as shown in Figure 20(b), and then stress-strain curve was identified by fitting the computed force-stroke curve with the measured force-stoke curve. The stroke is defined by the change of the 50mm gauge length (GL50mm) as shown in both Fig.20(a) and Fig.20(b). Figure 19(c) shows the plastic strain distribution computed by FEM and a very large strain concentrated at the center of the tensile specimen. Figure 21 represents the identified stress-strain curve based on well used swift hardening rule in which the initial yield stress, the strength coefficient and the strain hardening exponent are 524MPa, 1459MPa and 0.104, respectively. Using the identified stress-strain curve, the force-stroke curve (F_fem) reproduced by FEM was compared with the experimental curve (F_test) as shown in Figure 22. It can be seen that a good agreement between FEM and experimental measurement was obtained. Therefore, the identified stress-strain curve can be accepted for the computation of local stresses.

(a) Tensile specimen

(b) FE model
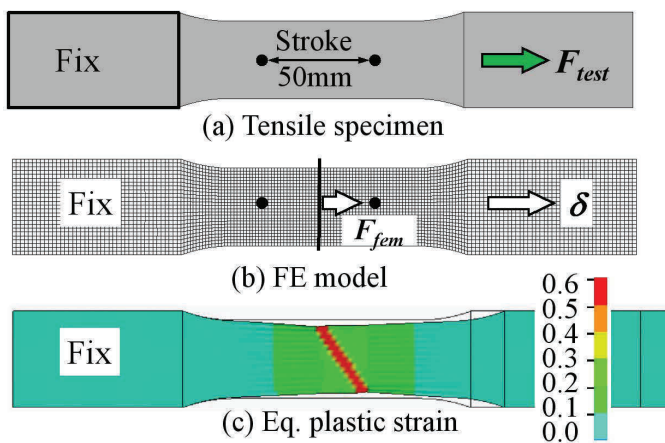
(c) Eq. plastic strain

Figure 20: Identification method of stress-strain relation.
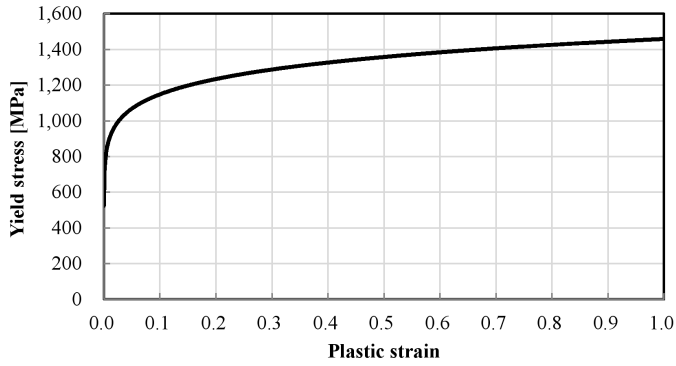
Figure 21: Identified stress-strain relation of 980MPa/t1.6mm steel sheet.
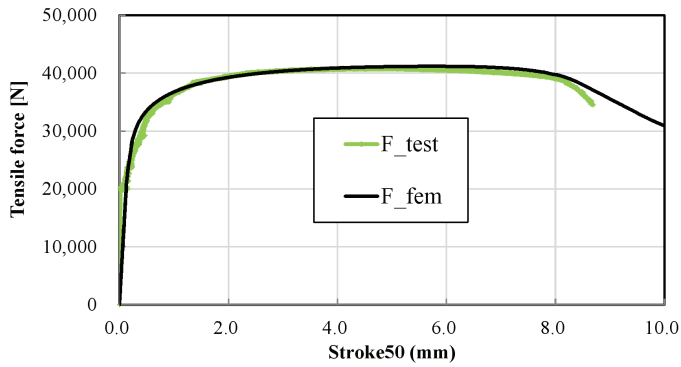

Figure 22: Comparison of force-stroke curves between FEM and experimental test.
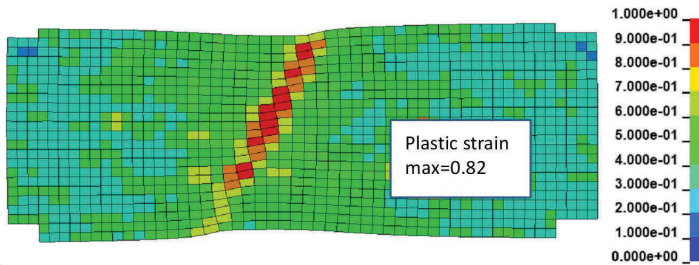

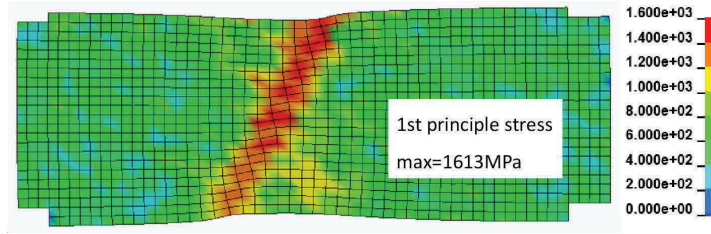Figure 23: Equivalent plastic strain.

Figure 24: The maximum principal stress.

Figure 23 and Figure 24 show the distributions of equivalent plastic strain and the maximum principal stress computed by M-FEM. From computed results, it can be easily observed that a large plastic strain and principal tensile stress exist at the center of the width direction of tensile test piece. Although the distributions of stress and strain in the low stress zones are not smooth enough due to the measuring errors, their effect is little in the large strain and high stress zone. The results can be considered reliable in general.

6   Damage distribution and damage limit identified by M-FEM

When both the stresses and the plastic strain are computed by M-FEM, various ductile damage values can be calculated following their damage rules. Here, the ductile damage C-value proposed by Cockcroft and Latham given by Eq.(12) is computed in which ε_f, σ_1 and $d\bar{\varepsilon}^p$ are the local fracture strain, the 1st principal stress and the equivalent plastic strain increment, respectively.

$$C = \int_0^{\varepsilon_f} \max(\sigma_1, 0) \cdot d\bar{\varepsilon}^p \tag{12}$$

Figure 25 shows the distribution of the ductile damage value in the tensile test piece. The maximum damage C-value is produced at the center of the large deformation band. This can be understood that the crack may be initiated at the center position more than the edges of the tensile test piece. The crack initiation position was also observed by experiments as shown in Figure 26, which verified the computed results of measurement based FEM. If the fracture section is observed in details, it can be seen the fracture face at the crack initiation position is perpendicular to the tensile direction.

When both the damage accumulation in the center element where the crack initiated shown in Fig.25 and the local tensile strain in the same element shown in Fig.11, are drawn by a graph, the historical change of the damage accumulation with the local strain during the tensile test can be represented by Figure 27. It can be seen

that the damage limit of high strength steel 980MPa/t1.6mm and the local fracture strain are 870MPa, 0.62, respectively.
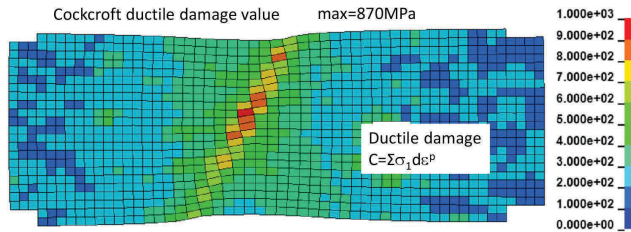

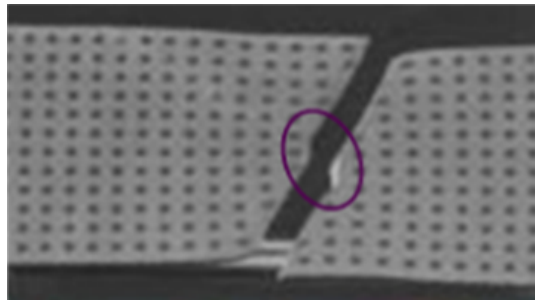Figure 25: Ductile damage value.
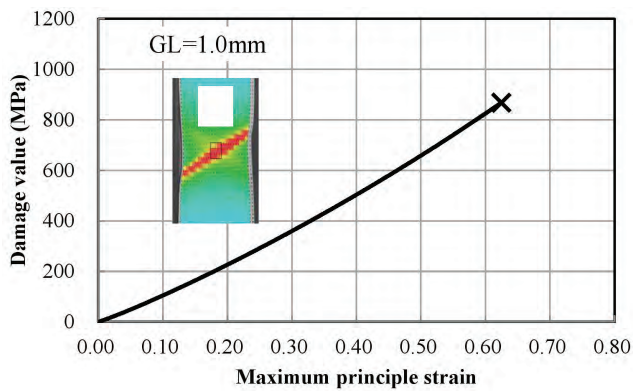

Figure 26: Crack initiation position.

Figure 27: Ductile damage accumulation at crack initiation element and its limit.

7 Local fracture strain and damage limit of various advanced high strength steels

As shown in Figure 28, the local strain path and local fracture strain for three advanced high strength steel sheets (1180MPa/t1.6mm, 980MPa/t1.2mm, 980MPa/t1.6mm) were measured with different grid pitch lengths (GL=2.0mm, 1.0mm, 0.5mm) in DIGM. Then, the damage limit was identified by the measurement based FEM. The mark "**+**" in this figure represents the local fracture strains when the crack initiated at the center of the tensile test pieces. The measured local fracture strain and identified damage limit for the three advanced high strength steel sheets (1180MPa/t1.6mm, 980MPa/t1.2mm, 980MPa/t1.6mm) are shown in Table 1. With the decreasing of grid pitch length, the local fracture strain and ductile damage limit increased. The damage limit measured based on a conventionally complicated Marciniak press test (1967) was also represented in Tab.1. The damage limit identified by the measurement based FEM agreed well with that measured by a conventional press test. The measuring method DIGM and developed measurement based FEM are accurate and reliable in analysis of the local mechanical behaviors such as local strains, local stresses and local damage of materials.
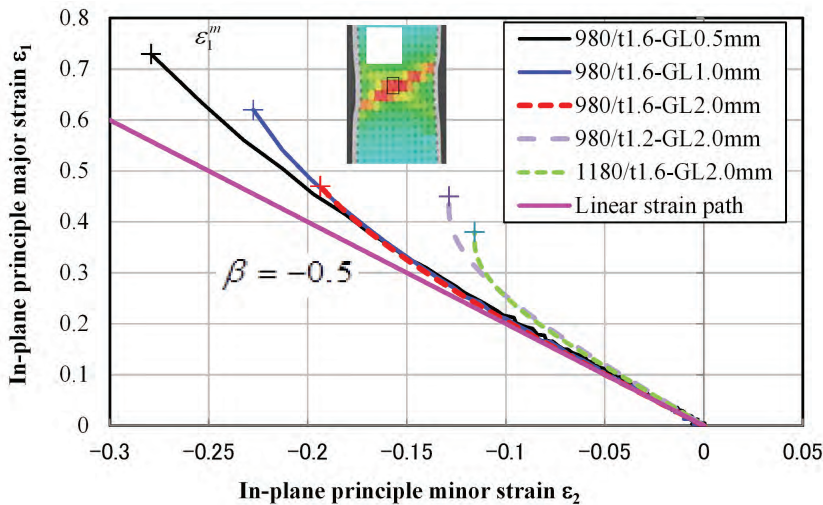

Figure 28: Local strain path and local fracture strain of advanced high strength steels.

Table 1: Local fracture strain and damage limit of advanced high strength steel sheets.

Advanced high strength steel sheets	GL (mm)	Local fracture strain	Damage limit (MPa) by tensile tests and M-FEM	Damage limit (MPa) by press test
980MPa/t1.6mm	0.5	0.73	1031.0	Not measured
980MPa/t1.6mm	1.0	0.62	870.3	Not measured
980MPa/t1.6mm	2.0	0.48	563.6	Not measured
980MPa/t1.2mm	2.0	0.47	611.6	612
1180MPa/t1.6mm	2.0	0.38	579.9	579

8   Summaries

(1) Displacement field in the uniaxial tensile test piece of advanced high strength steel sheets was successfully measured by digital image grid method (DIGM).

(2) A measurement based finite element method (M-FEM) for investigation of local strains, stresses and local damage of materials was developed.

(3) Local strains, stresses and damage distribution in uniaxial tensile test piece of 980MPa steel were computed by developed measurement based FEM.

(4) The maximum value of local principal strain, principal stress and ductile damage accumulation existed at the center of the width direction of the tensile test piece which was consistent with the crack occurrence position observed in experiments.

(5) The local fracture strain and damage limit of advanced high strength steel sheets (980MPa/t1.6mm, 980MPa/t1.2mm, 1180MPa/t1.6mm) were accurately measured by a uniaxial tensile test and identified by measurement based FEM compared with those measured by a conventional press test.

(6) The effect of grid pitch length on the ductile damage limit was investigated if different mesh sizes of FEM are employed in strength prediction. With the decreasing of grid pitch length, the ductile damage limit increased.

References

Chu, T. C.; Rasson, W. F.; Sutton, M. A.; Peters, W. H. (1985): Applications of digital-image-correlation techniques to experimental mechanics. *Experimental Mechanics,* vol. 25, pp. 232–244.

Cockcroft, M. G.; Latham, D. J. (1968): Ductility and the workability of metals. *Journal of the Institute of Metals,* vol. 96, pp. 33-39.

Coppieters, S.; Ichikawa, K.; Kuwabara, T. (2014): Identification of Strain

Hardening Phenomena in Sheet Metal at Large Plastic Strains. . *Procedia Engineering,* vol. 81, pp. 1288–1293.

Dupuy, J. S.; Lachuad, F.; Piquet, R.; Huet, J. (2010): Finite element model matching based on optical measurement fields on single shear lap joint. Annual conference proceedings of society for experimental mechanics, June 70-10, Indianapolis, Indiana, USA, 53-62.

Han, Z. D.; Atluri, S. N. (2014): Eshelby Stress Tensor T: a Variety of Conservation Laws for T in Finite Deformation Anisotropic Hyperelastic Solid & Defect Mechanics, and the MLPG-Eshelby Method in Computational Finite Deformation Solid Mechanics-Part I. *CMES,* vol. 97, no. 1, pp. 1-34.

Han, Z. D.; Atluri, S. N. (2014): On the (Meshless Local Petrov-Galerkin) MLPG-Eshelby Method in Computational Finite Deformation Solid Mechanics - Part II. *CMES,* vol. 97, no. 3, pp. 199-237.

Hopmann, C.; Klein, J. (2015): Determination of strain rate dependent material data for FEA crash simulation of polymers using digital image correlation. *Computational materials science, 100, Part B, April,* pp. 181–190.

Huang, G.; Yan, B.; Xia, Z. (2011): Measurement of r-values of High Strength Steels Using Digital Image Correlation. *SAE Int. J. Mater. Manuf.,* vol. 4, no. 1, pp. 385-395.

Lian, J.; Yang, H.; Vajragupta, N.; Münstermann, S.; Bleck, W. (2014): A method to quantitatively upscale the damage initiation of dual-phase steels under various stress states from microscale to macroscale. *Computational materials science,* vol. 94, November, pp. 245–257.

Liu, H. T.; Han, Z. D.; Rajendran, A. M.; Atluri, S. N. (2006): Computational Modeling of Impact Response with the RG Damage Model and the Meshless Local Petrov-Galerkin (MLPG) Approaches. *Computers, Materials & Continua,* vol.4, Issue 1, pp. 43-54.

Ma, N. (2013): Accurate simulation on failure and springback of sheet metal forming. *Sokeizai,* vol. 54, no. 4, pp. 21-26 (in Japanese).

Ma, N.; Takada, K; Sato, K. (2014): Measurement of local strain path and identification of ductile damage limit based on simple tensile test. . *Procedia Engineering,* vol. 81, pp. 1402-1407.

Marciniak, Z.; Kuczynski, K. (1967): Limit strains in the processes of stretchforming sheet metal International. *Journal of Mechanical Science,* vol. 9, pp. 609–620.

Pan, B.; Qian, K.; Xie, H.; Asundi, A. (2009): Two-dimensional digital image correlation for in-plane displacement and strain measurement : a review. *Measure-*

ment Science and Technology, vol. 20.

Paul, S. K. (2012): Micromechanics based modeling of Dual Phase steels: Prediction of ductility and failure modes. *Computational Materials Science,* vol. 56, April, pp. 34–42.

Peters, W. H.; Ranson, W. F. (1981): Digital imaging techniques in experimental stress analysis. *Optical Engineering,* vol. 21, pp. 27–431.

Ramazani, A.; Schwedt, A.; Aretz, A.; Prahl, U.; Bleck, W. (2013): Characterization and modelling of failure initiation in DP steel. . *Computational materials science,* vol.75, July, pp. 35-44.

Roux, S.; Hild, F. (2008): Ditigal image mechanical indentification, Experimental Mechanics, Doi:101007/s11340-007-9103-03.

Sato, J. (2006): Recovering multiplye view geometry from manual projections of multiply cameras. *Int. J. Comput.,* vol. 66, pp. 123-140.

Sato, K.; Yu, Q.; Hiramoto, J.; Urabe, T.; Yoshitake, A. (2015): A method to investigate strain rate effects on necking and fracture behaviors of advanced high-strength steels using digital imaging strain analysis. *Int. J. Imp. Eng.,* vol. 75, pp. 11-26.

Sladek, J.; Stanak, P.; Han, Z-D.; Sladek, V.; Atluri, S. N. (2013): Applications of the MLPG Method in Engineering & Sciences: A Review. *Computer Modeling in Engineering & Sciences,* vol. 92, Issue 5, pp. 423-475

Sutton, M. A. (1986): Application of an optimized digital correlation method to planar deformation analysis, Computer Vision/Computer Graphics Collaboration Techniques. *Computer Science,* vol. 4, pp. 143-150.

Takada, K.; Sato, K.; Ma, N. (2015): Fracture Prediction for Automotive Bodies using a Ductile Fracture Criterion and a Strain-Dependent Anisotropy Model. *SAE Int. J. Mater. Manuf.,* vol. 8, Issue 3.

Takuda, H.; Hama, T.; Nishida, K.; Yoshida, T.; Nitta, J. (2009): Prediction of forming limit in stretch flanging by finite element simulation combined with ductile fracture criterion. *Computer Methods in Materials Science,* vol. 9, no. 1, pp. 137-142.

Tarigopula, V.; Hopperstad, O. S.; Langseth, M.; Clusen, A. H.; Hild, F.; Lademo, O. G.; Eriksson, M. (2008): A study of large plastic deformations in dual phase steel using digital image correlation and FE analysis. . *Experimental Mechanics,* vol. 48, no. 2, pp. 181-196.

Ueda, Y.; Fukuda, K. (1989): New Measuring Method of Three-Dimensional, Residual Stresses in Long Welded Joints Using Inherent Strains as Parameters. *Trans. of the ASME, J. Eng. Materials and Technology,* vol. 111, pp. 1-8.

Yoneyama, S. (2011): Smoothing Measured Displacements and Computing Strains Utilising Finite Element Method. *Strain,* vol. 47, no. 2, pp. 258–266.

Zeng, D.; Xia, Z. (2010): Extending Tensile Curves beyond Uniform Elongation Using Digital Image Correlation: Capability Analysis. *SAE Int. J. Mater. Manuf.,* vol. 3, no. 1, pp. 702-710